

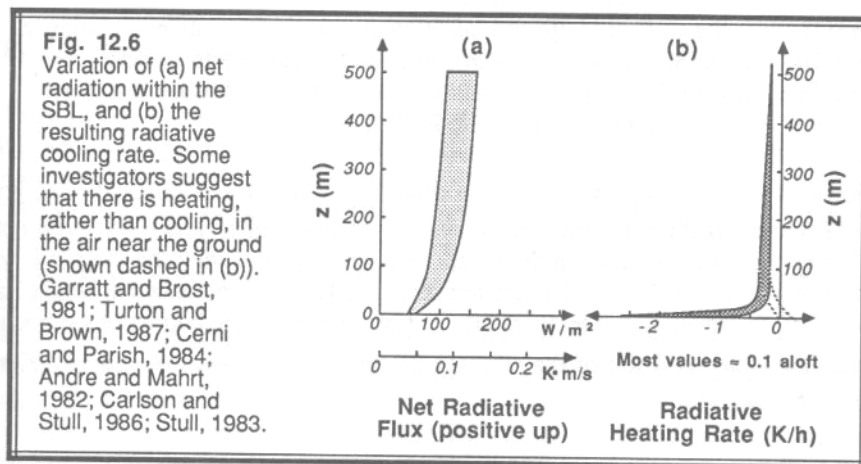
# Radiation and stable PBL

Hannu Savijärvi  
*University of Helsinki*

## 1. Introduction

The processes, which drive the stable BL (SBL), especially the nocturnal BL (NBL), are: radiation, turbulence, subsidence and advection (Stull 1988). We neglect here subsidence and advection; these can however be important in individual cases, especially during high pressures, and through cold drainage winds in hilly areas. A flat horizontally homogeneous clear-sky land NBL case is considered, in which turbulence is maintained by wind but is strongly suppressed by stability.

There is no solar radiation during the night. The downwelling longwave radiation  $F_{down}$  at the surface is typically 150-350 W/m<sup>2</sup> depending on temperature and humidity, while the upwelling LW flux from the ground ( $F_{up} = \epsilon_g \sigma T_g^4$ ) is 200-430 W/m<sup>2</sup>. Radiative cooling of the ground then occurs, driven by the net LW flux  $F_{net} = F_{up} - F_{down}$  being upward and about 50...80 W/m<sup>2</sup>. In the NBL, the typical upward increase of  $F_{net}$  causes small but significant LW cooling (0.1...0.3 K/h), since cooling by turbulence is small as well. The typical case for a clear midlatitude summer night is described in more detail in Section 4. First, we describe briefly the physics of LW radiation and some models for it.



## 2. LW physics and models

N<sub>2</sub> and O<sub>2</sub> molecules are transparent in thermal wavelengths (5-100 μm). Therefore, the clear-air up- and downwelling LW fluxes at each altitude  $z$  result from greenhouse gas molecules (like water vapour) emitting and absorbing at their air temperatures. The LW heating rate  $(\partial T / \partial t)_{LWR} = -(1 / \rho c_p)(\partial F_{net} / \partial z) = (g / c_p)(\partial F_{net} / \partial p)$  is proportional to the convergence of the net flux in the vertical. (There is also a similar horizontal flux convergence contribution, but it is small, and is 0 in the plane parallel approximation PPA of horizontal homogeneity). The local thermodynamic equilibrium LTE allows one to equate

emissivities and absorptivities by Kirchoff's law. PPA and LTE are excellent approximations in the NBL. A third good approximation is neglect of scattering. Although thermal scattering is in fact strong, it is also highly ineffective and so the absorption approximation (= no-scattering) works well, especially in clear air. Hence the transmissivity of a clear-air layer is closely equal to 1 – its emissivity (or 1 – its absorptivity).

The multi-atom greenhouse gas molecules exhibit lots of quantized vibrational and rotational states, and hence numerous emission and absorption lines in the thermal infrared. Water vapour molecules display a belt of vibrational lines at around 6.3  $\mu\text{m}$  (near-infrared) and a wide belt of strong rotational lines beyond 12  $\mu\text{m}$  (far-infrared). At 8-12  $\mu\text{m}$  the atmosphere is relatively transparent (LW window). The total flux transmissivity  $t(z, z')$  of an air layer  $z, z'$  is at each wavelength the product of transmittances by the existing, possibly overlapping lines, by the so-called continuum effect, and by clouds and aerosols. Clouds, aerosols and continuum “fill the window”: they emit/absorb in the LW window region, where the lines by atmospheric gases are mostly weak or nonexistent.

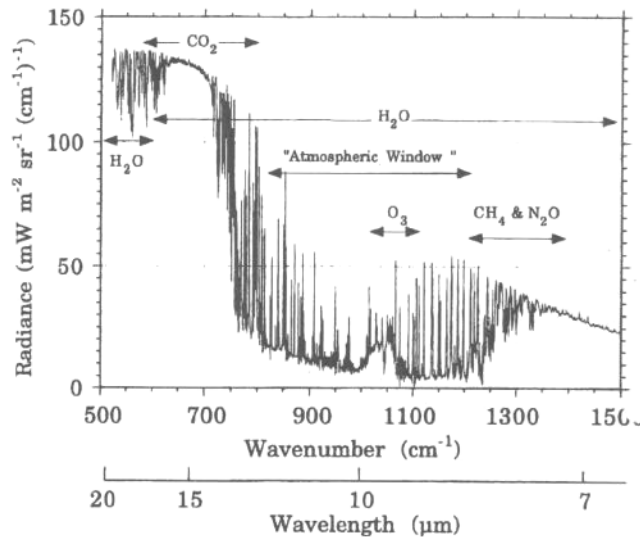


FIG. 3. Spectrum of zenith atmospheric emission measured by the Wisconsin spectrometer at 2000 UT on 6 December 1991.

The fluxes are formally the vertical and wavelength integrals of transmissivities x Planck functions through air columns above and below the height of interest  $z$ , plus boundary effects. Here, wave number  $k = 1/\lambda$  is used instead of wavelength  $\lambda$ , as is usual due to historic reasons. For each  $k$  one gets the spectral fluxes:

$$(1) \quad F_{k,down}(z) = \int_{\infty}^z \pi B_k(T(z')) \frac{dt_k(z, z')}{dz'} dz'$$

$$F_{k,up}(z) = [\varepsilon_k \pi B_k(T_s) + (1 - \varepsilon_k) F_{k,down}(0)] t_k(0, z) + \int_0^z \pi B_k(T(z')) \frac{dt_k(z, z')}{dz'} dz'$$

The downwelling flux typically increases downward as there are more and more e.g. water vapour molecules emitting, and their temperatures (hence the Planck function values  $B_k(T)$ ) also increase toward the surface. The upwelling flux consists of surface emission transmitted

but partly absorbed (the first r.h.s. term), plus upward radiation emitted by the air below  $z$  (the second term). The upward flux typically weakly decreases upward so the net flux increases upward, leading to LW cooling.

The calculation methods for the spectral integration vary a lot:

- 1) Line-by-line models (LBL) try to present the transmission by each spectral line for all relevant gases at very good spectral resolution through the whole LW spectrum. There are however millions of lines so this is too slow for any operational model. Can be used for reference, though. Each line follows a known simple analytic (Lorentz) shape, with line widths and strengths tabulated from fine-resolution laboratory measurements (e.g. HITRAN spectral data).
- 2) Band models use statistical averaging over narrow or wider wavenumber bands, which makes them much faster but slightly less accurate than LBLs. The main physics is still sound though, and all relevant gases can be included with realistic overlapping effects. Narrowband models ( $25\text{-}50\text{ cm}^{-1}\Delta k$ ) are considered fairly accurate. Depending on the assumptions for e.g. the line strength distributions, various ‘random band models’ such as Goody or Malkmus models may be constructed suitably for each gas.
- 3) The flux-emissivity methods average over the whole LW spectrum for each gas. They are very fast but must be tuned carefully as the physics is grossly simplified (for instance, overlapping, line broadening and continuum effects are crudely represented). They are especially good for demonstration, and for graphical diagrams.

The flux emissivity  $e$  of an air column is mostly dependent on its water vapour content. As a first approximation,  $e(\text{water vapour}) = 0.60 + 0.18\log(u^*)$ , where  $u^*$  is the pressure-scaled precipitable water content (in cm) of an air layer,  $u^* = \int q \left(\frac{p_0}{p}\right)^{0.85} \frac{dp}{g}$ . The scaling factor (where  $p_0$  is the air pressure of the lab spectral data, e.g., 1000 mb), takes crudely into account the very important fact that the emission/absorption lines are much wider in high pressures. The LBL and band models include the pressure broadening effect of absorption lines in a strict way based on kinetic gas theory.

Carbon dioxide is also a strong LW emitter/absorber but only in a relatively narrow vibrational band around  $15\text{ }\mu\text{m}$ . Hence its flux emissivity is at most 0.20, and its lines overlap strongly with those of water vapour. A warm and moist layer also exhibits a water vapour continuum effect, important in the LW window at  $8\text{-}12\text{ }\mu\text{m}$ , where there is little line absorption (except that of ozone in a narrow band around  $9.6\text{ }\mu\text{m}$ ). These effects are visually demonstrated in the included manuscript, via using a narrow band model, which has been validated against LBL results in a reference atmosphere.

The LW heating rate can be rewritten into a form with three terms. The dominating term describes cooling of the layer due to net IR emission to cold space (‘photon escape to space’, ‘cooling to space’). The second term describes cooling by net IR emission to cold ground. It is important during surface inversions. The third term describes net photon exchanges between

other air layers below and aloft. The net exchange term is usually small and is 0 in an isothermal atmosphere.

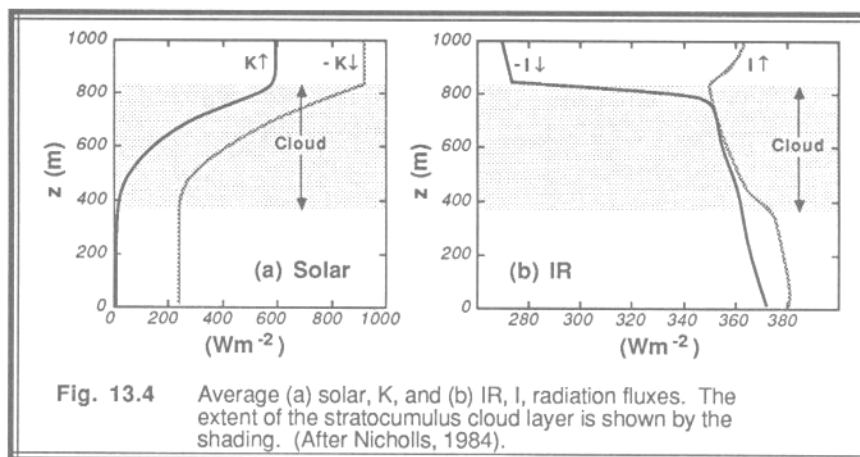
The HIRLAM clear-sky LW emissivity scheme neglects the third term (the Sasamori or local isothermal approximation), which makes this scheme extremely fast yet reasonably accurate for short-range forecasting. The ECMWF LW scheme is a 16-band Rapid Radiative Transfer Model (RRTM). It is based on lines sorted according to their strengths within each band (the so-called k-distribution method).

**Summary:** During clear skies, nighttime ground is cooling via a net upward LW flux at the surface, emitted IR photons escaping to space through the LW window. Also the NBL tends to cool radiatively, via net LW emission to space by the water vapour and carbon dioxide molecules. If there is a surface inversion, LW cooling is enhanced via photons also escaping to the cold ground. Inversion suppresses turbulence and makes LW radiation important in the nighttime surface and BL heat budgets.

### 3. Clouds

Clouds ‘fill all LW windows’; their emissivity is strong and nearly independent of wavelength (‘gray’). Hence the downwelling LW radiation typically increases when a low cloud covers the sky. We describe below the case for an overcast stratocumulus deck. By neglecting radiation from cloud sides and by weighting the radiation budget by the cloud cover, a scattered sky case can be handled crudely as well.

Flight observations (below) show the typical behaviour of the LW (and SW) fluxes across a sc deck. The downwelling LW flux increases rapidly at the cloud top due to droplet emission. Hence there is strong net flux divergence and LW cooling at the cloud top in about 30 m deep layer. The middle of a thick cloud is in a blackbody state, hence no LW cooling. In the base of the cloud the upward flux typically decreases into the cloud, so the cloud base tends to warm up by net absorbing the emission of the surface (if the surface is warmer than the cloudbase, as is usually the case).



The water cloud LW emissivity is approximately  $1 - \exp(-0.15 \text{ LWP})$  where LWP is the vertical cloud liquid water path (in g/m<sup>2</sup>). Even a thin water cloud (100 m thick) is close to a blackbody. Ice clouds are more transparent as the ice particles are much larger than water droplets and the ice contents are typically much smaller than the water contents of warm clouds.

Aerosol particles (other than cloud) are usually so optically thin that they seldom have any effect in the longwave. An exception might be a strongly polluted inversion layer, where many particles are kept trapped.

#### **4. Typical behaviour of a NBL:**

##### **Radiative and turbulent heating rates in the clear-air boundary layer**

**Hannu Savijärvi  
Division of Atmospheric Sciences  
University of Helsinki**

(Manuscript submitted to QJRMS, 5.4.2005)

##### *Summary*

The diurnal evolution of a clear-sky midlatitude summertime boundary layer (BL) was studied using a column model over smooth and homogeneous land, subject to weak, moderate, and strong winds. The high-resolution BL model (lowest point at 30 cm) was equipped with an adequate turbulence scheme and a narrow band LW radiation scheme, the latter validated using ICRCM data.

In off-line ICRCM experiments ground emissivity  $\varepsilon < 1$  lead to extra LW cooling of air near the surface compared to  $\varepsilon = 1$ . However, much stronger LW cooling at 1-3 m heights, and warming below 1 m, was obtained by setting the ground colder than air at screen height; a typical condition during clear nights. Conversely, a warm surface anomaly typical of sunny days lead to strong LW warming at 1-3 m heights, with LW cooling just above ground. These ground temperature anomalies dominated the LW heating/cooling patterns up to 3-4 m heights, perhaps explaining controversies in the observed LW flux divergences close to the ground.

Interactive model results indicate that the middle part of a windy clear-air nocturnal BL is dominated by turbulent cooling while the upper and lower NBL is dominated by LW cooling instead. Close to the cold ground (below about 1 m), a fourth layer is formed with LW warming and turbulent cooling, in good agreement with the off-line LW experiments. LW cooling dominates turbulent cooling in the whole NBL (except near the surface), when the 10 m mean winds fall below about 1-1.5 m/s. In these light wind conditions the Monin-Obukhov theory should be revised to include radiative effects.

In clear-air daytime conditions strong convective BL heating dominates over weak LW cooling except at 1-3 m heights where the cooler air absorbs the thermal emission by the hot ground. The LW warming of this superadiabatic surface layer appears to be strong enough to induce local turbulent cooling (despite the hot surface) in an 'hour glass' pattern independently of wind speed such that the total diabatic heating rate remains nearly constant in height.

Keywords: turbulent fluxes, radiative fluxes, nocturnal boundary layer, convective surface layer

## 1. Introduction

The structure of the stable nocturnal boundary layer (NBL) is not well known. The factors for the nocturnal cooling of air, leading to strong stability, are according to Stull (1988): horizontal advection, vertical motion, turbulence, and longwave radiation. Observational studies can rarely cover all these factors simultaneously with good accuracy. Hence their results have been quite variable, to the extent that even the sign of the longwave radiative heating is controversial near the surface (Stull 1988). On the other hand, numerical NBL simulations have suffered from low vertical resolution and inaccurate LW radiation schemes. For instance, Zhong and Fast (2003) claim that the main source for the surface nighttime forecast error in three state-of-the-art mesoscale models was their LW schemes.

Many observational and model studies have shown that longwave radiative flux divergence may contribute significantly to the nocturnal clear-air cooling (e.g. Garratt and Brost 1981, André and Mahrt 1982, Estournel and Guedalia 1985, Gopalakrishnan et al. 1998, Tjemkes and Duynkerke 1989, Sun et al. 2003). On the other hand, LW flux convergence (i.e. LW warming) has been observed by Funk (1960) and Nkemdirim (1978) close to the ground. Räisänen (1996) and Ha and Mahrt (2003) have pointed out that the LW flux calculations are extremely sensitive to subtle changes in the temperature and moisture profiles near the surface. High accuracy, high vertical resolution and realistic profiles are therefore necessary in theoretical and model studies.

The role of turbulence is generally thought to be a cooling one near the surface in a clear-sky NBL, because the ground is cooler than the air (e.g. Howell and Sun 1999). The turbulence is governed by wind speed. Yet some model studies have indicated strong turbulent heating at 2-3 m heights for many geostrophic wind speeds (e.g. Gopalakrishnan et al. 1998, Rama Krishna et al. 2003). This heating was compensated by an even stronger LW cooling, in direct opposition with Funk's observations. In any case, if the radiative heating or cooling is significant compared to turbulence, then the Monin-Obukhov similarity principle, on which the present surface layer turbulence theories are based, is violated, as pointed out by Sun et al. (2003). The surface layer may therefore need a particularly close look.

In the present model-based study, we simulate the typical diurnal cycle of the clear-air midlatitude summer boundary layer by using an one-dimensional atmospheric boundary layer (ABL) model as e.g. in Rama Krishna et al. (2003), but using very high vertical and temporal resolution. The model is equipped with a fairly accurate LW radiation scheme and with an adequate turbulence scheme. Advection and vertical motion are omitted, so the diurnal evolution of temperature is driven only by turbulence and radiation. The test case is based on observations in a flat, smooth and horizontally homogeneous environment (U.S. Midwest) so local advection and vertical motion should not be significant near the surface. The data provide realistic initial values and validation for moderate winds. Experiments are made with several geostrophic wind speeds from 0.5 to 20 m/s.

## 2. The ABL model

Our ABL model is a column version of the University of Helsinki (UH) mesoscale model. The prognostic model equations (for the horizontal wind components, potential temperature and specific humidity) are standard. They are e.g. the same as eqs (1-4) in Rama Krishna et al. (2003). Surface temperature is predicted via a five level soil thermal diffusion scheme (Savijärvi 1992) while the soil moisture content is kept constant such that the Bowen ratio is close to 1 during daytime in the present simulations. The references below contain the details of the model so only a brief description of the clear-air parameterizations is given.

The turbulence scheme is based on the Monin-Obukhov similarity theory in the lowest model layer. Aloft, vertical diffusion coefficients for momentum and scalars depend on wind shear and squared mixing length. The mixing length follows the Blackadar formulation with the asymptotic mixing length being 150 m. Stability is introduced via a factor  $f(Ri)$ , where  $Ri$  is the local bulk Richardson number. In unstable conditions ( $Ri < 0$ ) Dyer-Businger forms are used for  $f(Ri)$  while in stable conditions  $f(Ri) = 1 - 5Ri$  for both momentum and scalars, being 0.1 in very stable conditions. The same  $f(Ri)$  are used in all layers as there are several model levels within the surface layer at any time due to high vertical resolution.

Such a mixing length ('Blackadar')-type turbulence scheme has been among the best, especially in NBL conditions, in recent comparisons with observations and TKE-based algorithms (Hess and Garratt 2002, Zhang and Zheng, 2004). The turbulence scheme has produced results (in the UH mesoscale model) in agreement with

observations of basic variables and turbulent fluxes from aircraft and towers in many different environments, from tropical Pacific and Africa (Savijärvi 1997, Savijärvi and Matthews 2004), Midwest U.S. (Savijärvi 1991), northwest China (Savijärvi and Jin 2002), over boreal forests (Savijärvi and Amnell 2001), coastal zones (Savijärvi 2004) and sea ice (Vihma and Brümmer 2002), to even the Mars Viking and Pathfinder lander sites (Savijärvi and Siili 1993, Savijärvi et al. 2004).

The shortwave radiation scheme is here based on the rapid algorithm used in HIRLAM (Savijärvi 1990). It has agreed fairly well with observations (Mejgaard et al. 2001, Niemelä et al. 2001). The LW scheme is described and validated in the next section.

The relevant model parameters and input data are presented in the next sections. Vertical levels are in the present experiments at 0.3, 1, 3, 10, 22, 50, 100, 170, 250, ... ,20000 m above the ground. High vertical resolution near the ground calls for small time steps, 10 s is used in the present experiments.

### 3. The longwave radiation scheme

The longwave radiation scheme calculates the upwelling and downwelling LW fluxes ( $F_{up}$ ,  $F_{down}$ ) at each altitude from solutions to the plane-parallel equation of radiative transfer, using the absorption approximation with a diffusivity factor of 1.66, and assuming local thermodynamic equilibrium. The spectral fluxes at each wavenumber  $k$  (or in a narrow band) are obtained from

$$(1) \quad \begin{aligned} F_{k,down}(z) &= \int_{\infty}^z \pi B_k(T(z')) \frac{dt_k(z, z')}{dz'} dz' \\ F_{k,up}(z) &= \left[ \varepsilon_k \pi B_k(T_s) + (1 - \varepsilon_k) F_{k,down}(0) \right] t_k(0, z) + \int_0^z \pi B_k(T(z')) \frac{dt_k(z, z')}{dz'} dz' \end{aligned}$$

where  $B_k(T)$  is the Planck function,  $T_o$  the surface temperature (at roughness height  $z_{oh}$ ) and  $\varepsilon_k$  the ground emissivity.  $t_k$  is the LW flux transmissivity of air layer  $z-z'$ , due to the presence of water vapour, carbon dioxide and ozone in variable amounts. The main computational problem is how to represent the strong spectral variation of  $t_k$  for millions of quantized absorption/emission lines of the greenhouse gases in each air layer.

A line-by-line calculation would be far too slow in an interactive model. A statistical narrow band model representation (NBM) for  $t_k$  was therefore adopted. Our NBM covers the 0-1200  $cm^{-1}$  wavenumber range in 48 bands, the 1200-2100  $cm^{-1}$  range in 18 bands and the 2100-2500  $cm^{-1}$  range in one band so there are 67 bands in the LW range. The band parameters for water vapour, carbon dioxide and ozone are taken from Houghton (1992). Goody random band model is adopted for water vapour while Malkmus model is used for carbon dioxide and ozone. Curtis-Godson method is used for the very important line pressure broadening along vertical paths while the Roberts et al. (1976) method is adopted for the water vapour continuum. The LW heating rate of air is calculated from the vertical convergence of the total net LW flux  $F_{net} = F_{up} - F_{down}$ . Thus at each altitude  $z$

$$(2) \quad \left( \frac{\partial T}{\partial t} \right)_{LWR}(z) = -\frac{1}{\rho C_p} \frac{\partial}{\partial z} (F_{up} - F_{down}) = \frac{1}{C_p} \frac{\partial F_{net}}{\partial p}$$

Here  $\rho$  is density of air and  $C_p$  is its specific heat at constant pressure  $p$ .

It is important to validate the NBM results against line-by-line (LBL) reference calculations. Some comparisons are collected to Table 1, which shows key LW flux values using the ICRCCM mid-latitude summer (MLS) profiles for temperature, water vapour and ozone (Ellingson et al. 1991). Included are also values from the Clough et al. (1992) line-by-line model, which is equipped with a comprehensive scheme for water vapour

continuum. Table 1 shows that the NBM is within the (narrow) scatter of the LBL results and is very close to the 35 model median of the ICRCCM.

For illustration, Fig. 1 shows the spectral clear-air MLS fluxes from the NBM at the surface and at 10 km for  $\varepsilon=1$ . The upwelling surface flux is simply the ground blackbody emittance while the downwelling flux demonstrates water vapour continuum partly filling the LW window at 800-1200  $cm^{-1}$  (12-8  $\mu m$ ) with nearly black areas mostly due to water vapour lines on both sides. At 10 km, above most of the air moisture, water vapour effects are evident only in the strongly absorbing far infrared (0-400  $cm^{-1}$ ) while signatures of carbon dioxide and ozone are seen at around 700  $cm^{-1}$  (15  $\mu m$ ) and 1050  $cm^{-1}$  (9.5  $\mu m$ ), respectively. The net flux is the area between the curves in Fig.1. Its increase upward produces LW cooling (via Eq. 2), which amounts to  $(\partial T / \partial t)_{LWR} = -2$  K/day on the average for the MLS 0-10 km layer.

#### 4. Some test cases

##### (a) The effect of surface emissivity

Some off-line introductory tests are now carried out using the NBM. We first demonstrate, as in Varghese et al. (2003), the effect of (grey) ground emissivity  $\varepsilon$  for the cooling rates very near the surface, using the MLS profile. All gases are here active (as in nature) while Varghese et al. (2003) included only water vapour.

The MLS profile was defined in Ellingson et al. (1991) at 1 km intervals in the lower atmosphere (e.g.  $T(0) = 294.0$  K,  $T(1 \text{ km}) = 290.0$  K). The air temperatures and gas concentrations are now additionally interpolated linearly to 0.1, 0.3, 1, 3, 10, 30, 100 and 300 m. Figure 2 shows the resulting LW heating rate profile up to 30 km, for  $\varepsilon = 1.0$  and  $\varepsilon = 0.8$ . Note the logarithmic vertical scale, which accentuates conditions near the surface. The  $\varepsilon = 1$  profile is identical to the LBL results at 1 km and aloft. Near the surface the  $\varepsilon = 1$  profile approaches a constant value of about  $-3.8$  K/day) in Fig. 2, in accordance with radiative transfer theory. For  $\varepsilon = 0.8$ , LW cooling is however enhanced near the surface, heating rate being up to  $-9.5$  K/day in the lowest 0 - 0.1 m layer. The extra cooling due to low ground emissivity decays upward, its effect extending to about one kilometre according to Fig. 2.

The effect was similar in Varghese et al. (2003). It is however slightly weaker in our calculation, which also includes carbon dioxide and ozone. As LW emissivities of about 0.96 are typical for most natural grounds (instead of 0.8), the emissivity effect may not be the dominant factor for the nocturnal near-surface LW cooling of air.

##### (b) Cold and hot ground

In the above comparisons the ground was at the same temperature as the air at the surface. In reality however the ground is slightly colder than air at screen height (2 m) during clear nights, while the reverse is true during clear days. Räisänen (1996) demonstrated (using sonde data) that such a discontinuity may have a big impact near the surface. Ground made 3 K colder than air at 2 m lead to strong LW cooling in the lowest 30 m, up to 30 K/day near the surface. He only showed one case, however, with a strong surface inversion in the lowest 100 m. The top of this inversion was also cooling strongly (12 K/day) by LW net flux divergence.

The ground temperature is now set 1 K colder than air at the surface ( $dT = -1$  K) in our NBM calculations with MLS air profiles ( $\varepsilon = 1$  and all gases active). Consequently there is a sharp and shallow 1 K step change (an unresolved surface temperature inversion) across the lowest 10 cm. This leads to a very strong LW cooling (Fig. 3, dotted line). The cooling rate is 157 K/day for the lowest 0-10 cm layer and decays nearly logarithmically up to about 30 m height.

Such a sharp 'step' discontinuity is, of course, unrealistic. We therefore distribute the discontinuity to the air temperatures via an exponential decay:  $T(z) = T(z, \text{MLS}) + dT \exp(-z/H)$ , where  $H$  is an adjustable scale height. For  $H = 0.1$  m the inversion extends to about 0.3 m, and for  $H = 1$  m, to about 3 m. A similar procedure for potential temperature was suggested by Ha and Mahrt (2003). The LW heating rates for  $H$  of 0.1 m and 1 m are

shown in Fig. 3. There is LW cooling at the top of each inversion, the cooling being the stronger the shallower the inversion is. Moreover, there is LW warming above the cool surface (up to the respective scale height) in those cases where the surface inversion is resolved by at least two grid points. Physically, the warm top of the inversion tends to cool by net emitting toward the colder surface, while the lower, colder air layers (if resolved by the grid) tend to warm up by net absorbing the emission from aloft. These findings are similar to Räisänen's, who applied a logarithmic T-profile between the surface and 2 m.

If the above exercises are repeated applying instead a warm ground anomaly ( $dT = +1$  K) typical of daytime, the effects on the LW heating rates (Fig. 4) are simply mirror imaged about the vertical. Consequently, there is LW cooling in a shallow layer just above the warm ground where the warm near-surface air layers net emit upward. Aloft, there is LW warming as the cooler air is readily absorbing the warm emission. Above about 30 m the surface discontinuity has no effect anymore.

Despite the quite strong local heating/cooling rates shown in Figs. 3-4, the associated flux changes from the  $dT = 0$  case are only of the order of 0.1 W/m<sup>2</sup> in the lowest metres, and even less higher up. Therefore, these effects are very hard to obtain using flux measurements, since the measurement errors are typically much larger.

In summary, Figs. 3-4 demonstrate that the LW heating rates close to the ground are quite sensitive to the ground temperature deficit/surplus and to the temperature profiles near the surface. They are relatively less sensitive to the ground emissivity (Fig. 2), although low emissivities do lead to systematic cooling near the surface.

These off-line sensitivity tests with fixed temperature and gas concentration profiles are illustrative but academic in the sense that the strong LW heating/cooling rates naturally act to modify the temperatures continuously, together with turbulence. Also the water vapour concentration varies near the surface, due to turbulence, evaporation and dew formation. Hence interactive ABL model experiments are needed. These are described in the following. In the model, the turbulence and the SW and LW radiation schemes are called at full accuracy every short time step (10 seconds) so the danger for inaccuracy due to nonlinear instabilities or infrequent updating of radiative heating (Pauluis and Emanuel 2004) should be minimal.

## 5. Interactive experiments

The present ABL model experiments simulate a typical diurnal cycle above the U.S. Midwest plains in summertime. The case is based on data in Rama Krishna et al. (2003) for 16-17 June 1980 at Kincaid, Illinois, where a plume-validation experiment resulted in a lot of observations. The sky was clear, winds and moisture were moderate and the 2 m temperatures varied from 283 K in the morning (0500 local solar time, 05 LT) to 295 K in the afternoon (15 LT). Sunrise was at about 0450 LT and the sun set at about 1910 LT.

The model was initialized via the 12 LT T,Td sounding and the parameter values were set appropriate for the observation site, an open grassy field. Thus, for instance, latitude is 39.6 N, roughness lengths 0.10 m, surface albedo, 0.20, and surface emissivity, 0.96. Specific humidity was predicted while carbon dioxide (360 ppmv) and ozone (MLS profile) were fixed. With geostrophic wind set to the observed 6 m/s, the simulations stay within 1 K of the observed hourly 2 m temperature evolution and the soundings presented in Rama Krishna et al. (2003). The simulated surface (10 m) winds are 2 - 3.5 m/s as are the observed, and the simulated and observed upper-BL winds exhibit a weak nocturnal jet peaking at about 00-01 LT. The simulated 2 m relative humidities are 30...75% as observed, and specific humidities stay around 7 g/kg in the lower boundary layer.

The predicted soil surface temperature  $T_o$  reaches 298 K at 14 LT and goes down to 281 K by 04 LT. The difference  $T_o - T_{2m}$  ( $dT$  of Section 4.2) is about +3 K around midday, and -1...-2 K during the night. The observed  $T_o$  -values are not known, but based on the good fit of the 2 m simulated temperatures to the observed one may assume that the modeled surface temperatures may not be too far off from the true radiometric surface temperatures.

### (a) ABL during moderate winds

Figure 5 displays the results for  $V_g = 6$  m/s. Shown are potential temperature profiles at 07, 12, 19 and 24 LT (top panel), instantaneous heating rate profiles in the convective boundary layer at 07 and 12 LT (mid panel), and heating rates for the evening and midnight (nocturnal) boundary layer at 19 and 24 LT (bottom panel). The vertical axis is logarithmic, for accentuation of results near the surface, and also for demonstration of possible logarithmic behavior (or loss thereof) in the surface layer. The near-surface turbulent and LW heating rates at each hour are additionally shown in Tables 2-3, which confirm that the displayed heating rates at 12 LT and 24 LT are rather typical for the daylight and nighttime hours while the 07 LT and 19 LT heating rates characterize the shorter morning and evening transition periods, when the stability is changing rapidly in the surface layer.

Figure 5 shows well-mixed daytime potential temperature profiles up to 1500 m with a strongly superadiabatic surface layer (to about 10 m) in the midday 12 LT profile (Values at 0.1 m ( $= z_{0h}$ ) are  $T_o$  predicted for the ground). An inversion extends up to about 100 m at 19 LT, and to 400 m, by 24 LT above the cooling ground. The nocturnal inversion has grown up to about 500 m by 07 LT while a growing early-morning convective layer characterizes the lowest 100 m. Residuals of the old mixed layer are seen above the surface inversions at 19, 24 and 07 LT. The behavior of the diurnal clear-sky boundary layer is quite typical and the values were close to the available observations. The simulated  $\Theta$ -profiles are fairly logarithmic in  $z$  in the lowest 5-10 meters down to the ground.

The mid panel of Fig. 5 shows that the turbulent heating rate is quite strong in the shallow but rapidly growing convective layer at 07 LT while that at 12 LT is strong between 50 m and 1000 m and at the surface. The LW radiative heating rates are weak and mainly negative. However, between 0.5 m and 10 m the midday LW heating rate is strongly positive (up to 25 K/day) while the turbulent heating rate is relaxed, even negative. The ‘hour glass’ pattern suggests that the midday superadiabatic layer is maintained by LW warming. Close to the warm ground (below 0.5 m) the LW heating rates are clearly negative. They display a clear resemblance to the profiles shown in Fig. 4 for a warm surface. The SW radiative heating of air is small (max 2 K/day during midday, not shown) and is not important.

The bottom panel of Fig. 5 shows the NBL heating rates during the evening transition and midnight hours. At 19 LT, strong turbulent cooling of windy air clearly dominates below 50 m but this slows down quickly (c.f. Table 3). At 24 LT turbulent cooling dominates the layer 50-400 m and near the ground (below 5 m), where the vertical wind shear is strong. On the other hand, the LW heating rates of 19 LT and 24 LT are rather similar to each other, indicating strongish radiative cooling (5-7 K/day) at 5-30 m, weaker cooling higher up, and LW warming just above the cool ground. The near-surface profiles are quite similar to those in Fig. 3 for a cold surface anomaly. These LW heating profiles agree with the observed nocturnal radiative flux convergences (LW warming) reported very near the surface (below 1-3 m), and divergences (LW cooling) higher up, discussed in the Introduction.

According to Fig. 5, turbulent cooling dominates in the middle of a well-developed NBL under moderate winds. LW cooling is however equally important in the 5-50 m layer, and it actually dominates near the top of the NBL and aloft. This three-layer thermodynamic structure is similar to that found e.g. by Garratt and Brost (1982,  $V_g = 10$  m/s) and Rama Krishna et al. (2004,  $V_g = 3-9$  m/s). We may now add a new, fourth layer: Close to the surface, below about 1-2 m, cold ground leads to strong LW warming, and to even stronger turbulent cooling.

Turbulence is however strongly dependent on wind speed. Hence we will now vary the geostrophic wind speed, keeping everything else unchanged in the model experiments.

### (b) ABL during strong and weak winds

The case of strong wind,  $V_g = 20$  m/s, is shown in Fig. 6. The surface (10 m mean) wind is here 8-9 m/s during the day and 6-7 m/s during nighttime. The ground and the BL air remains therefore cooler during daytime and slightly warmer during nighttime than with the more moderate winds of Fig. 5, as can be expected. The BL is also higher and better mixed at all times and no residual layer can be distinguished above the nocturnal inversion in the  $\Theta$ -profiles (top panel). The morning and midday heating rate profiles (mid panel) indicate dominance of convective heating over weak LW radiative cooling throughout the windy convective layer.

During the evening transition period, cooling of the near-surface air is dominated by vigorous turbulence (bottom panel). Strong winds keep the fully-developed lower NBL relatively well-mixed and neutral, and the associated small vertical gradients reduce the turbulent cooling to nearly zero at 1-10 m by 24 LT. Hence the four-layer thermodynamic structure is very clear in the windy NBL at 24LT, with LW cooling dominating near the top and also at the bottom 1-30 m, while in the mid-NBL (30-800 m) turbulent cooling dominates instead. Just above the surface there is moderate turbulent cooling and weak LW warming induced by the cool surface. Note that the surface temperature deficits/surpluses over the 2 m temperatures ( $dT$ ) are small in Fig. 6 (due to strong wind) and hence the surface anomaly effects remain relatively small in the near-surface LW heating rates in this case.

Finally, Fig. 7 displays the interesting case of weak winds,  $V_g = 1.5$  m/s. Here the surface winds are about 1.3 m/s during the day and 0.7-0.8 m/s during the night. The daytime boundary layer nevertheless grows up to 1.5 km in conditions that here approach free convection. The ground then cools rapidly toward midnight through strong net radiative loss, with strong vertical temperature gradients developing in the near-surface air (top panel). Note a large negative  $T_o - T_{2m}$  (about  $-3$  K) at 24 LT near the ground in Fig. 7. The nocturnal inversions remain low. They extend to about 150 m at 24 LT, and to about 300 m by 07 LT with a residual layer aloft.

The heating rate profiles of the convective phase (mid panel) are rather similar to the windier cases, testifying the dominance of convective heating, except in the strongly superadiabatic surface layer at around 1 m, which warms up by absorbing thermal radiation emitted by the warm layers and the hot surface below.

In the light-wind clear-air NBL (bottom panel), the turbulent heating rates are small except very near the surface, hence LW cooling dominates everywhere above about 1 m height. The LW heating rates amount to  $-12$  K/day ( $-0.5$  K/h) at 3-10 m heights at 24 LT. The cold ground at 24 LT ( $dT$  being about  $-3$  K) leads to strong LW heating just above it. This is compensated by even stronger turbulent cooling in a very shallow layer at the ground.

If  $V_g$  is decreased further, the above patterns remain the same in our simulations and amplify. Based on Figs. 5-7, one can therefore state that if surface wind is less than about 1-1.5 m/s, nocturnal LW cooling will dominate over turbulent cooling, except very near the surface.

## 6. Conclusions and discussion

The structure and diurnal evolution of a clear-air midlatitude summertime boundary layer was studied using a numerical column model over smooth and homogeneous grassland, subject to weak, moderate, and strong winds. The high-resolution ABL model was equipped with a slow but fairly accurate narrow band LW radiation scheme, which was validated using ICRCCM data.

In off-line experimenting using the ICRCCM midlatitude summer atmosphere ground emissivity  $\varepsilon < 1$  lead to some extra cooling of air near the surface compared to  $\varepsilon = 1$ . However, much stronger LW cooling at 1-3 m heights, and warming below 1 m, was obtained by setting the ground colder than air at screen height (2 m); a typical condition during clear nights. The cooling is due to the screen-level air net emitting toward the colder ground, while the warming close to the ground is caused by the cooler air net absorbing the emission by the slightly warmer inversion air aloft. The ground temperature deficit dominates the LW heating/cooling pattern up to 3-4 m heights.

Conversely, a warm surface anomaly typical of sunny days leads to strong LW warming at 1-3 m heights, with LW cooling just above the warm ground. These surface effects may explain the controversial results about nocturnal LW flux divergence very near the surface discussed in the Introduction: The magnitude and even the sign of the LW heating close to the ground depends critically on the measurement (or lowest grid point) height, and on the actual temperature deficit of the ground relative to the air temperature.

The ABL model with its lowest grid point at 30 cm and  $z_{0h}$  at 10 cm was then applied without advection and subsidence effects for a June clear-sky case in the U.S. Midwest plains. The diurnal temperature evolution was well simulated. The results for moderate and strong winds were in fair agreement with previous studies, which

have indicated that the middle part (0.1h...0.8h, h being the BL height) of the nocturnal BL is dominated by turbulent cooling while the upper and lower NBL is dominated by LW cooling instead. This three-layer structure of the windy NBL was most evident during strong winds ( $V_g$  20 m/s, Fig. 6). The present high-resolution NBL experiments indicate furthermore that near the cold ground, below about 1 m, a fourth layer is formed with LW warming and turbulent cooling. This is in good agreement with the off-line LW experiments and low-level LW observations.

The model-produced potential temperature profiles across the lowest 2-3 m are nearly logarithmic. An alternative analytic representation for the near-surface NBL temperature profile is that the temperature deficit between the surface and 2 m decays exponentially upward with a scale height of about 1 m.

The nocturnal LW cooling rate profiles were fairly similar from hour to hour in the simulations, cooling increasing with increasing negative curvature in the near-surface temperature profile as in Ha and Mahrt (2003). The LW cooling profiles are insensitive to wind speed but the NBL turbulence decays with decreasing wind. At some point LW cooling therefore begins to dominate in the whole NBL (Sun et al. 2003). According to the present experiments this takes place when the surface (10 m) wind speed falls below about 1-1.5 m/s. In these light wind conditions the Monin-Obukhov theory should be revised to include the radiative effects. Furthermore, since the surface temperature deficit is large during light winds, the fourth-layer shallow LW effects become strong and clear. It should be added that the present light wind experiments appear to be the first of their kind, since all earlier ABL model studies have considered geostrophic wind speeds of at least 3 m/s.

In contrast, in the morning and midday clear-sky convective conditions the turbulent heating rate profiles are fairly similar for all wind speeds. Strong convective heating dominates over weak LW cooling except very near the surface during midday and early afternoon. Here, thermal emission by the hot ground gets absorbed by the cooler air at 1-2 m heights. The subsequent LW warming of the shallow superadiabatic layer appears to be strong enough to induce local weak turbulent cooling in an 'hour glass' fashion so that the total diabatic heating rate remains nearly constant in height.

Finally, it is interesting to note that daytime surface temperature surpluses (over 1 m air temperatures) of up to 30 K at 12 LT, and nighttime deficits of about 5 K have now definitely been observed by the thermal emission spectrometers (mini-TES) on board the NASA Mars rovers (Smith et al. 2004). This was predicted by Savijärvi et al. (2004), who also showed that these surface effects lead to responses in the Martian LW heating rates, which are basically similar to (although much stronger than) those shown in the present article. In the thin and rapidly responding Martian atmosphere, the main radiatively active constituents are carbon dioxide and dust.

#### **Acknowledgements:**

This work is related to the EU Marie Curie Chair Project MEXC-CT-2003-509742 and the Academy of Finland projects 167836, 178457, 144030, 174918. Some of the calculations were made in the Centre for Scientific Computing (CSC), Espoo, Finland.

Table 1. Downwelling and upwelling radiative fluxes ( $Wm^{-2}$ ) at the surface and at the tropopause for the ICRCCM midlatitude summer atmosphere, with water vapour only (with and without continuum), and with all gases (water vapour, 300 ppmv of CO<sub>2</sub>, ozone). Surface emissivity is 1.0. The upwelling flux is 423.62  $Wm^{-2}$  at the surface.

MLS profiles (ICRCCM, Ellingson et al. 1991)	Surface, down	Tropopause, up	Tropopause, down
Water vapour lines only:			
ICRCCM LBL range (3 models)	266-268		
Clough et al. LBL (1992)	269.0	335.8	6.9
Present NBM	266.8	333.0	6.3
Water vapour with continuum:			
LBL range	320-330		
Clough et al. LBL (1992)	333.8	321.3	7.4
Present NBM	324.0	326.4	7.4
All gases active:			
LBL range	340-345		
ICRCCM median (35 models)	343.4	291.2	22.1
Present NBM	344.9	291.0	22.4

Table 2. Instantaneous longwave radiative heating rates (K/day) at each hour (local solar time, LT) in the lowest gridpoints during a diurnal simulation with Vg of 6 m/s. Sun rises at about 0450 LT and sets at about 1910 LT.

hr \ z:	0.3 m	1 m	3 m	10 m	22 m	50 m	100m	170m	250m	350m	500m
01	12.4	1.9	-2.0	-4.0	-4.8	-4.5	-4.0	-3.5	-3.2	-3.1	-2.6
02	11.6	1.7	-2.0	-3.8	-4.6	-4.3	-3.8	-3.4	-3.1	-3.1	-2.6
03	10.9	1.5	-2.0	-3.7	-4.5	-4.2	-3.7	-3.3	-3.1	-3.0	-2.6
04	10.2	1.4	-2.0	-3.7	-4.3	-4.0	-3.6	-3.2	-3.0	-3.0	-2.6
05	7.6	0.9	-1.3	-2.7	-3.7	-3.7	-3.4	-3.0	-2.9	-2.9	-2.6
06	-4.7	-2.2	-1.6	-1.0	-1.0	-1.6	-2.1	-2.3	-2.5	-2.6	-2.4
07	-11.1	2.9	2.9	0.7	-1.2	-1.6	-1.4	-1.2	-1.6	-2.2	-2.1
08	-14.5	11.2	9.2	4.3	0.3	-1.2	-1.6	-1.7	-1.5	-1.6	-1.8
09	-16.0	19.9	15.1	7.6	1.7	-0.5	-1.3	-1.6	-1.8	-2.0	-1.7
10	-17.0	26.1	19.4	9.9	2.7	0.0	-1.0	-1.4	-1.7	-2.0	-1.8
11	-18.9	28.3	21.3	11.1	3.3	0.3	-0.8	-1.3	-1.6	-2.0	-1.8
12	-21.0	26.7	20.8	11.0	3.3	0.3	-0.8	-1.2	-1.6	-1.9	-1.8
13	-19.4	27.0	21.3	11.6	3.9	0.8	-0.4	-0.9	-1.3	-1.6	-1.5
14	-19.3	23.6	18.8	10.1	3.1	0.3	-0.7	-1.1	-1.5	-1.8	-1.6
15	-18.6	16.2	13.8	7.4	1.9	-0.2	-1.0	-1.2	-1.5	-1.8	-1.6
16	-16.7	8.0	7.8	3.9	0.4	-1.0	-1.4	-1.5	-1.7	-1.9	-1.7
17	-12.6	-0.4	0.9	-0.3	-1.5	-1.9	-1.9	-1.8	-1.9	-2.1	-1.8
18	-5.1	-6.2	-5.3	-4.6	-3.8	-3.1	-2.5	-2.2	-2.1	-2.2	-1.9
19	6.3	-3.6	-6.3	-7.0	-6.3	-4.8	-3.6	-2.8	-2.5	-2.4	-2.1
20	16.1	3.4	-4.0	-7.5	-7.5	-5.9	-4.5	-3.4	-2.9	-2.7	-2.1
21	16.7	4.0	-2.9	-6.2	-6.8	-5.8	-4.7	-3.8	-3.2	-2.8	-2.3
22	15.8	3.5	-2.4	-5.3	-6.1	-5.4	-4.6	-3.8	-3.3	-3.0	-2.4
23	14.6	2.9	-2.2	-4.6	-5.5	-5.0	-4.4	-3.8	-3.4	-3.1	-2.5
24	13.4	2.3	-2.1	-4.2	-5.1	-4.7	-4.1	-3.6	-3.3	-3.1	-2.5

Table 3. Instantaneous turbulent heating rates (K/day) at each hour (local solar time, LT) in the lowest gridpoints during a diurnal simulation with Vg of 6 m/s.

hr \ z:	0.3 m	1 m	3 m	10 m	22 m	50 m	100m	170m	250m	350m	500m
01	-17.8	-7.8	-4.5	-3.7	-3.7	-4.6	-5.7	-6.1	-4.9	-3.3	-1.3
02	-15.7	-6.5	-3.3	-2.2	-2.4	-3.2	-4.5	-4.7	-4.7	-3.3	-1.7
03	-14.1	-5.1	-2.2	-1.2	-1.2	-2.6	-3.6	-4.1	-4.2	-3.4	-2.0
04	-13.1	-4.6	-1.7	-0.7	-0.9	-1.8	-2.9	-3.7	-3.6	-2.9	-2.1
05	29.1	28.7	22.7	6.7	0.9	-1.5	-2.4	-2.8	-3.0	-2.9	-2.1
06	72.9	60.9	52.2	43.1	33.4	12.5	0.3	-3.2	-3.2	-2.4	-2.1
07	73.7	48.9	42.2	40.2	39.9	38.8	37.3	11.5	-3.4	-3.3	-1.8
08	68.6	34.8	31.4	32.8	34.9	34.1	31.9	28.3	24.7	19.9	-4.4
09	55.1	12.4	13.3	18.3	23.1	24.5	24.8	24.9	25.3	25.8	25.8
10	45.7	-0.8	3.4	11.1	17.4	19.4	19.8	19.5	19.2	18.3	16.5
11	37.8	-10.2	-4.0	5.4	12.9	15.2	16.2	16.3	16.2	16.2	15.4
12	29.9	-16.3	-9.9	0.0	7.8	10.5	11.7	12.4	12.7	12.8	12.5
13	31.0	-12.9	-5.5	5.3	13.6	17.1	18.6	19.2	19.9	20.4	20.6
14	21.9	-15.8	-7.9	2.5	10.5	13.8	15.7	16.3	16.9	17.5	17.7
15	6.6	-20.8	-13.7	-4.2	2.2	5.5	7.0	7.8	8.4	8.8	9.0
16	-4.5	-19.9	-13.8	-6.2	-0.9	2.0	3.3	4.1	4.7	5.4	5.9
17	-18.3	-20.4	-14.2	-7.6	-3.8	-1.5	-0.4	0.5	1.2	1.8	2.4
18	-38.0	-28.9	-22.3	-14.6	-9.5	-4.7	-3.2	-2.0	-1.3	-0.8	-0.3
19	-79.4	-61.4	-48.3	-26.1	-15.7	-7.9	-3.7	-1.3	-0.1	0.0	-0.1
20	-51.3	-38.0	-29.8	-24.0	-19.5	-13.8	-7.4	-3.2	-1.2	0.0	0.1
21	-38.6	-26.0	-19.4	-16.9	-15.2	-13.3	-9.8	-5.5	-2.5	-0.3	0.1
22	-30.2	-18.2	-12.8	-12.0	-11.2	-10.9	-9.6	-6.9	-4.0	-1.6	-0.3
23	-24.3	-13.1	-8.8	-8.3	-7.8	-8.6	-8.4	-7.1	-4.9	-2.2	-0.7
24	-20.2	-9.9	-5.9	-5.4	-5.4	-6.5	-7.0	-6.7	-5.1	-2.9	-0.9

## References

- André, J.-C., and L. Mahrt 1982: The nocturnal surface inversion and influence of clear-air radiative cooling. *JAS*, 39, 864-878.
- Clough, S. A., M. J. Iacono, and J.-L. Moncet, 1992: Line-by-line calculations of atmospheric fluxes and cooling rates: Application to water vapor. *JGR*, 97, D14, 15761-15785.
- Estournel, C., and D. Guedalia, 1985: Influence of geostrophic wind on atmospheric nocturnal cooling. *JAS*, 38, 2695-2698.
- Ellingson, R. G., J. Ellis, and S. Fels, 1991: The intercomparison of radiation codes used in climate models: Long wave results. *JGR*, 96, D5, 8929-8953.
- Funk, J. P., 1960: Measured radiative flux divergence near the ground at night. *QJRMS* 86, 382-389.
- Garratt, J. R., and R. A. Brost, 1981: Radiative cooling effects within and above the nocturnal boundary layer. *JAS*, 38, 2730-2746.
- Gopalakrishnan, S. G., M. Sharan, R. T. McNider, and M.P. Singh, 1998: Study of radiative and turbulent processes in the stable boundary layer under weak wind conditions. *JAS*, 55, 954-960.
- Ha, K. J., and L. Mahrt, 2003: Radiative and turbulent fluxes in the nocturnal boundary layer. *Tellus*, 55A, 317-327.
- Hess, G. D., and J. Garratt, 2002: Evaluating models of the neutral barotropic planetary boundary layer using integral measures: Part II. Modelling observed conditions. *BLM*, 104, 359-369.
- Houghton, J. T., 1992: *The physics of atmospheres*, 3rd ed., Cambridge University Press, 203 pp.
- Howell, J. F., and J. Sun, 1999: Surface layer fluxes in stable conditions. *BLM*, 90, 495-520.
- Niemelä, S., P. Räisänen and H. Savijärvi 2001: Comparison of surface radiative flux parameterizations: Part II: Shortwave radiation. *Atmospheric Research*, 58, 141-154.
- Nkemdirim, L. C., 1978: A comparison of radiative and actual nocturnal cooling rates over grass and snow. *JAM*, 17, 1643-1646.
- van Meijgaard, E., U. Andrae, and B. Rockel, 2001: Comparison of model predicted cloud parameters and surface radiative fluxes with observations on the 100 km scale. *Meteorol.Atmos.Phys.*, 77, 109-130.
- Pauluis, O., and K. Emanuel, 2003: Numerical instability resulting from infrequent calculation of radiative heating. *MWR*, 132, 673-686.
- Rama Krishna, T., M. Sharan, S. G. Gopalakrishnan, and Aditi, 2003: Mean structure of the nocturnal boundary layer under strong and weak wind conditions: EPRI case study. *JAM*, 42, 952-969.
- Roberts, R. E., J. E. A. Selby, and L. M. Biberman, 1976: Infrared continuum absorption by atmospheric water vapour in the 8-12  $\mu\text{m}$  window. *Appl.Opt.*, 15, 2085-2090.
- Räisänen, P., 1996: The effect of vertical resolution on clear-sky radiation calculations: Tests with two schemes. *Tellus*, 48A, 403-423.
- Savijärvi, H., 1990: Fast radiation parameterization schemes for mesoscale and short-range forecast models. *JAM*, 20, 437-447.

- Savijärvi, H., 1991: The United States Great Plains diurnal ABL variation and the nocturnal low-level jet. *MWR*, 119, 833-840.
- Savijärvi, H., 1992: On surface temperature and moisture prediction in atmospheric models. *Beitr.Phys.Atmosph.*, 65, 281-292.
- Savijärvi, H., and T. Siili, 1993: The Martian slope winds and the nocturnal PBL jet. *JAS* 50,77-88.
- Savijärvi, H. 1997: Diurnal winds around Lake Tanganyika. *QJRMS*, 123, 883-899.
- Savijärvi, H., and T. Amnell, 2001: High resolution flight observations and numerical simulations: horizontal variability in the wintertime boreal boundary layer. *Theoretical and Applied Climatology*, 70, 245-252.
- Savijärvi, H., and L. Y. Jin, 2001: Local winds in a valley city. *BLM*, 100, 301-319.
- Savijärvi, H., 2004: Model predictions of coastal winds in a small scale. *Tellus*, 56A, 287-295.
- Savijärvi, H., and S. Matthews, 2004: Flow over small heat islands: a numerical sensitivity study. *JAS*, 61, 859-868.
- Savijärvi, H., A. Määttänen, J. Kauhanen, and A.-M. Harri, 2004: Mars Pathfinder: New data and new model simulations. *QJRMS*, 130, 669-684.
- Smith, M. D. et al., 2004: First atmospheric science results from the Mars Explorations Rovers Mini-TES. *Science*, 306, 1750-1753.
- Stull, R. B., 1988: *An Introduction to Boundary Layer Meteorology*. Kluwer Academic, Boston, 666 pp.
- Sun, J., S. P. Burns, A. C. Delany, S. P. Oncley, T. W. Horst, and D. H. Lenschow, 2003: Heat balances in the nocturnal boundary layer during CASES -99. *JAM*, 42, 1649-1666.
- Tjemkes, S. A., and P. G. Duynkerke, 1989: The nocturnal boundary layer: Model calculations compared with observations. *JAM*, 28, 161-175.
- Varghese S., A. S. V. Murthy, and R. Narasimha, 2003: A fast, accurate method of computing near-surface longwave fluxes and cooling rates in the atmosphere. *JAS*, 60, 2869-2886.
- Vihma, T., and B. Brümmer, 2002: Observations and modeling of on-ice and off-ice flows in the northern Baltic Sea. *BLM*, 103, 1-27.
- Zhang, D. L., and W. Z. Zheng, 2004: Diurnal cycles of surface winds and temperatures as simulated by five boundary layer parameterizations. *JAM*, 43, 157-169.
- Zhong, S., and J. Fast, 2003: An evaluation of the MM5, RAMS and Meso-Eta models at subkilometer resolution using VTMX field campaign data in the Salt Lake Valley. *MWR*, 131, 1301-1323.

Figure captions:

Fig. 1. Upwelling and downwelling spectral radiative fluxes ( $Wm^{-2}(cm^{-1})^{-1}$ ) from the narrow band model for the midlatitude clear-air summer atmosphere with surface emissivity of 1.0. The net flux is the area between the curves.

a) At surface pressure (1013.25 hPa)    b) At 10 km height

Fig. 2. The longwave heating rate profile (K/day) from the NBM for MLS with surface emissivity 1.0 (solid line), and 0.8 (dashed line). Note the logarithmic vertical scale.

Fig. 3. The LW heating rate profile (K/day) from the NBM (MLS, surface emissivity 1.0), for surface temperature deficit of 1 K.

Fig. 4. Same as Fig. 3 but for surface temperature surplus of 1 K

Fig. 5. Vertical profiles from diurnal clear-air ABL simulations. Moderate wind;  $V_g = 6$  m/s.

Top panel: Potential temperature (K) at 07, 12, 19 and 24 LT.

Mid panel: Turbulent heating (solid) and LW heating (dashed, K/day) at 07 and 12 LT.

Bottom panel: Turbulent heating and LW heating at 19 and 24 LT.

Fig. 6. Same as Fig. 5 but for strong wind,  $V_g = 20$  m/s.

Fig. 7. Same as Fig. 5 but for weak wind,  $V_g = 1.5$  m/s.

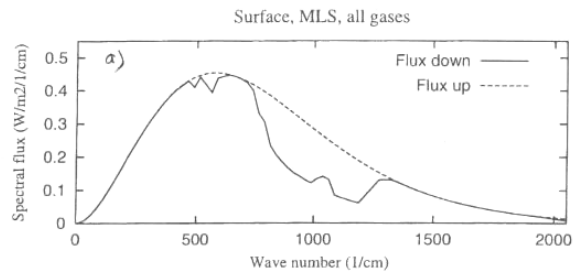


Fig. 1

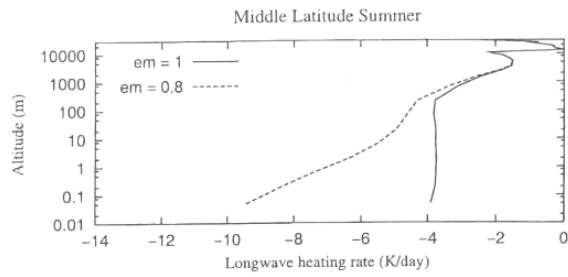
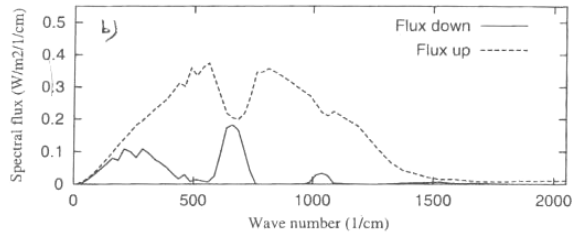


Fig. 2

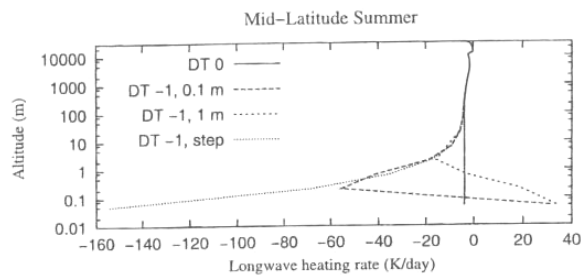


Fig. 3

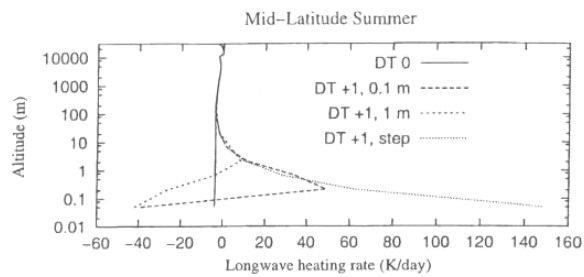


Fig. 4

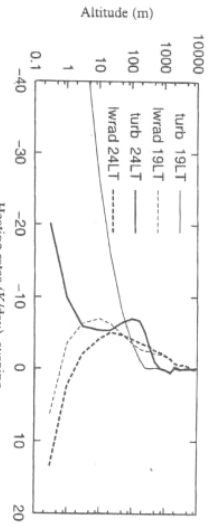
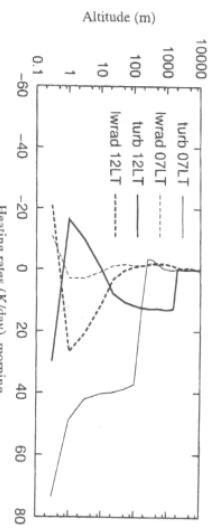
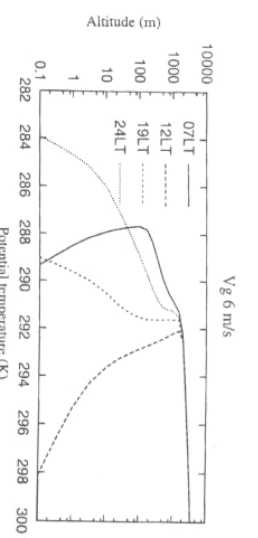
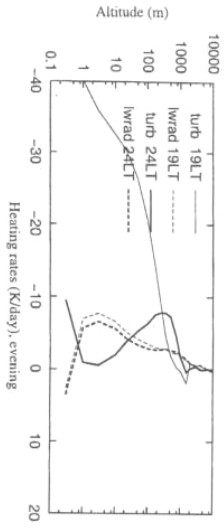
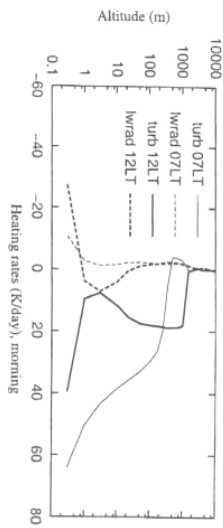
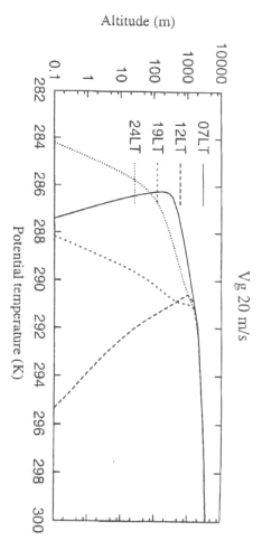
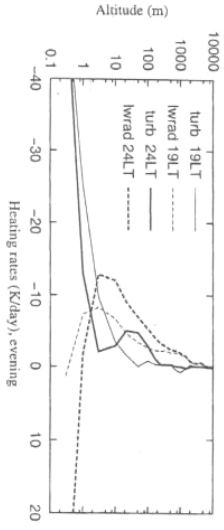
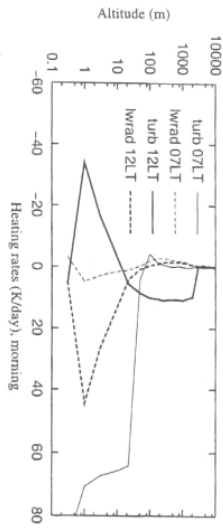
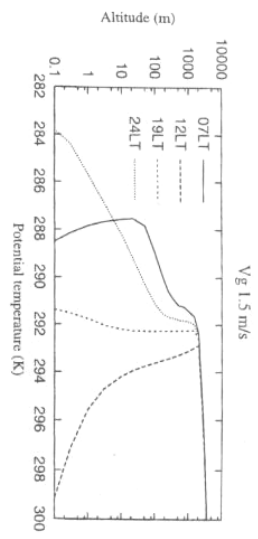


Fig. 7

Fig. 6

Fig. 5

